RESEARCH ARTICLE | JULY 03 2025

Self-corrected hemodynamic analysis of blood viscosity for detection of endothelial injury in atherosclerosis using magnetic resonance imaging FREE

Haiwei Shan ; Shizhen Chen; Xiaodong Zhang; Haidong Li; Lei Shi; Xin Zhou

Physics of Fluids 37, 071905 (2025)
https://doi.org/10.1063/5.0270151

Physics of Fluids ARTICLE pubs.aip.org/aip/pof

Self-corrected hemodynamic analysis of blood viscosity for detection of endothelial injury in atherosclerosis using magnetic resonance imaging

Cite as: Phys. Fluids **37**, 071905 (2025); doi: 10.1063/5.0270151
Submitted: 10 March 2025 · Accepted: 25 April 2025 ·
Published Online: 3 July 2025

Haiwei Shan,[1,2] Shizhen Chen,[3,4] Xiaodong Zhang,[1,2] Haidong Li,[3,4] Lei Shi,[3,4] and Xin Zhou[1,3,4,a)]

AFFILIATIONS

[1]State Key Laboratory of Digital Medical Engineering, Key Laboratory of Biomedical Engineering of Hainan Province, School of Biomedical Engineering, Hainan University, Sanya 572024, China
[2]MRI Center, School of Biomedical Engineering, Hainan University, Sanya 572024, China
[3]State Key Laboratory of Magnetic Resonance Spectroscopy and Imaging, National Center for Magnetic Resonance in Wuhan, Wuhan Institute of Physics and Mathematics, Innovation Academy for Precision Measurement Science and Technology, Chinese Academy of Sciences, Wuhan 430071, China
[4]University of Chinese Academy of Sciences, Beijing 100049, China

[a)]**Author to whom correspondence should be addressed:** xinzhou@wipm.ac.cn

ABSTRACT

Carotid atherosclerosis remains a leading cause of stroke, where hemodynamic forces such as wall shear stress (WSS) plays a critical role in plaque formation. WSS strength depends on blood viscosity, yet current quantification methods neglect individual variations driven by metabolic disorders (e.g., diabetes and hyperlipidemia). This oversight masks early endothelial dysfunction preceding visible plaque formation. Herein, we propose an *in vivo* viscosity estimation framework, personalized blood viscosity (PBV), which integrates hemodynamic pressure-flow measurements and viscosity calculation. PBV-corrected WSS analysis demonstrates endothelial injury lesions in high-fat diet animals can be seen at 2–3 weeks before plaque formation. By linking the hyperlipidemia-driven viscosity shifts to WSS anomalies, this present study establishes a paradigm shift from geometric to personalized rheological assessment, suggesting a novel method for early atherosclerosis risk stratification in clinic.

I. INTRODUCTION

Atherosclerosis (AS) is a chronic vascular inflammatory condition. It originates from the pathological remodeling of arterial walls driven by hemodynamic disturbances and endothelial dysfunction.[1,2] Hemodynamic forces, particularly wall shear stress (WSS)—the tangential frictional force exerted by blood flow—play a pivotal role in regulating vascular homeostasis.[3–8] Clinically, sustained low WSS triggers mechano-sensitive pathways (e.g., PECAM-1/Piezo1 activation, PYK2 upregulation, and eNOS phosphorylation at inhibitory Tyr657 sites), leading to nitric oxide (NO) deficiency and endothelial dysfunction—a hallmark of early AS pathogenesis.[9–14] A recent study has shown that the low wall shear stress condition also promotes the generation of neutrophil extracellular traps by downregulating Piezo1 expression to imbalance intracellular Ca^{2+} concentrations and increase HDAC2 expression, which participates in atherosclerosis by directly mediating organ and endothelial toxicity.[15]

While computational fluid dynamics (CFD) and 4D flow MRI have advanced WSS quantification for evaluating plaque dynamics,[16,17] critical limitations persist in accounting for blood viscosity—a rheological parameter with dual regulatory roles in WSS: (1) viscosity directly modulates shear stress magnitude via the Newtonian relation, and (2) viscosity indirectly modulates shear stress magnitude via the flow resistance alteration. These modulations are nonlinear and too complex to predict.[18] Emerging evidence suggests that blood and plasma viscosities may contribute to AS progression in systemic metabolic disorders such as diabetes or hyperlipidemia.[19] However, current WSS analyses frequently overlook these dynamic viscosity variations by relying on empirical values or *in vitro* measurements.[20,21]

There are two critical challenges of blood viscosity strategies on WSS quantification. First, common viscometers (e.g., cone-plate viscometers) fail to replicate *in vivo* hemodynamic conditions, particularly under disease-specific shear rate conditions.[22,23] Second, the WSS differences among various regions are the most likely cause of the discrete and focal nature of the AS lesions. However, how the blood viscosity and WSS environment deteriorates during the progression from diabetes or hyperlipidemia to AS has not been explored completely.[24] This methodological gap hinders the identification of viscosity-sensitive WSS thresholds predictive of early AS which is a crucial need for preventive diagnostics.[25]

To address these limitations, a blood viscosity estimating method called Personalized Blood Viscosity (PBV) estimation was proposed in the present study. PBV estimation can integrate traditional WSS quantification methods for measuring the viscosity-sensitive WSS in arteries. Unlike conventional approaches, PBV incorporates three innovations: (1) PBV estimation provides the possibility to noninvasively measure blood viscosity *in vivo*. (2) With the non-Newtonian viscosity fitting, PBV estimation can integrate into CFD or 4D-flow MRI methods as a viscosity module. (3) PBV-corrected WSS quantification method may highlight low WSS regions, which is confirmed by histological results. The present study achieves the technical scheme in the *in vivo* measurement of blood viscosity, reveals the potential influence of blood viscosity change on plaque formation in the early stage of AS, and provides a framework for precision hemodynamic assessment in early AS risk stratification.

II. MATERIALS AND METHODS

A. Personalized blood viscosity estimation

Figure 1 illustrates the workflow for PBV estimation and WSS correction. The core of this method is to calculate the blood viscosity using the *in vivo* velocity field in the laminar flow region and extend to the upstream and downstream for WSS quantification.

Due to the degree of freedom in the curvature of the cervical spine, it is always possible to find a segment composed of the left common carotid artery (LCCA) with a bending angle of less than 4.6°. Previous studies by Cherry and Eaton have shown that the circumferential component of blood flow velocity can be ignored at this bending angle.[26] Under this premise, mass conservation can be expressed as

$$\frac{\partial u_r r}{r\partial r}+\frac{\partial u_z}{\partial z}=0, \tag{1}$$

and axial momentum can be expressed as

$$\rho\left(\frac{\partial u_z}{\partial t}+u_r\frac{\partial u_z}{\partial r}+u_z\frac{\partial u_z}{\partial z}\right)=-\frac{\partial p}{\partial z}+\mu\left(\frac{1}{r}\frac{\partial}{\partial r}\left(r\frac{\partial u_z}{\partial r}\right)+\frac{\partial^2 u_z}{\partial z^2}\right), \tag{2}$$

where p represents the pressure, t represents the time, ρ represents the blood density, and μ represents the viscosity. The subscripts r and z indicate the radial and axial components of velocity vector u. For the voxel i, the expression for shear rate is defined as follows:

$$\gamma_i=\left(\frac{\partial u_z}{\partial r}\right)_i. \tag{3}$$

The pulse wave of blood vessels can be approximately obtained from the changes in the cross-sectional area of blood vessels on both upstream and downstream sides. Concurrently, the influence of the vessel's motion boundary on the blood flow is addressed as follows:[27]

$$\frac{dA}{dp}=const \Longleftrightarrow \frac{p(t)-p_s}{A(t)-A_{\max}}=\frac{p_s-p_d}{A_{\max}-A_{\min}}, \tag{4}$$

$$u_r(r=R)=\frac{dR}{dt}, \tag{5}$$

where A and R represent the area and radius of the cross section, respectively. p_s and p_d represent the systolic and diastolic blood pressure, respectively.

Furthermore, for the numerical solution of μ_i and γ_i across all voxels, the common no-slip boundary condition must be introduced

$$u_z(r=R)=0. \tag{6}$$

The mappings $(r_i,z_i,t_i)\rightarrow\gamma_i$ and $(r_i,z_i,t_i)\rightarrow\mu_i$ are obtained through the solution process, which allows for the plotting of μ-γ scatter plots. To interact with CFD solvers, these mappings need to be converted into a non-Newtonian viscosity curve $\mu(\gamma)$ by fitting. Because the power-law viscosity model does not require additional input empirical parameters, in this study, a power-law fluid model with undetermined coefficients was employed, with the expression as follows:

$$\mu_i=\begin{cases}\mu(\gamma_{\max}) & \gamma_i\geq\gamma_{\max},\\ \alpha\gamma_i^{\beta} & \gamma_{\min}<\gamma_i<\gamma_{\max}\\ \mu(\gamma_{\min}) & \gamma_i\leq\gamma_{\min}.\end{cases} \tag{7}$$

The undetermined coefficients α and β are the key parts that need to be fitted. To make the fitting results represent more regions in the cross section, it is necessary to assign the area weights to each point in the μ–γ scatterplot. A series of home-made semi-automatic MATLAB scripts (Ver. R2022a) were developed to achieve the aforementioned estimation process.

According to the procedures outlined above, a solver that can calculate non-Newtonian viscosity in the LCCA based on the combination of blood and vascular motion behavior with blood pressure has been implemented. Correspondingly, the empirical power-law viscosity used by Mendieta *et al.* in Ref. 28 is introduced in the present report as a comparison of traditional methods with the expression of the following equation:

$$\mu_i(Pa\cdot s)=\begin{cases}0.025 & \gamma_i\leq 0.0931\ s^{-1},\\ 0.01467\gamma_i^{-0.2245} & 0.0931\ s^{-1}<\gamma_i<631\ s^{-1},\\ 0.00345 & \gamma_i\geq 631\ s^{-1}.\end{cases} \tag{8}$$

B. Animal experiments

To validate the robustness of PBV estimation in arteries of various sizes and investigate the influence of blood viscosity changes caused by hyperlipidemia on the WSS before plaque formation, cross-species animal experiments are necessary. 25 male SD rats, weighing 100–120 g each, were housed in groups of five in clean cages of an SPF facility. They were maintained under a 12:12-h light/dark cycle in humidity- and temperature-controlled rooms, with *ad libitum* access to food and water. After 7 days of adaptation, the rats were randomly

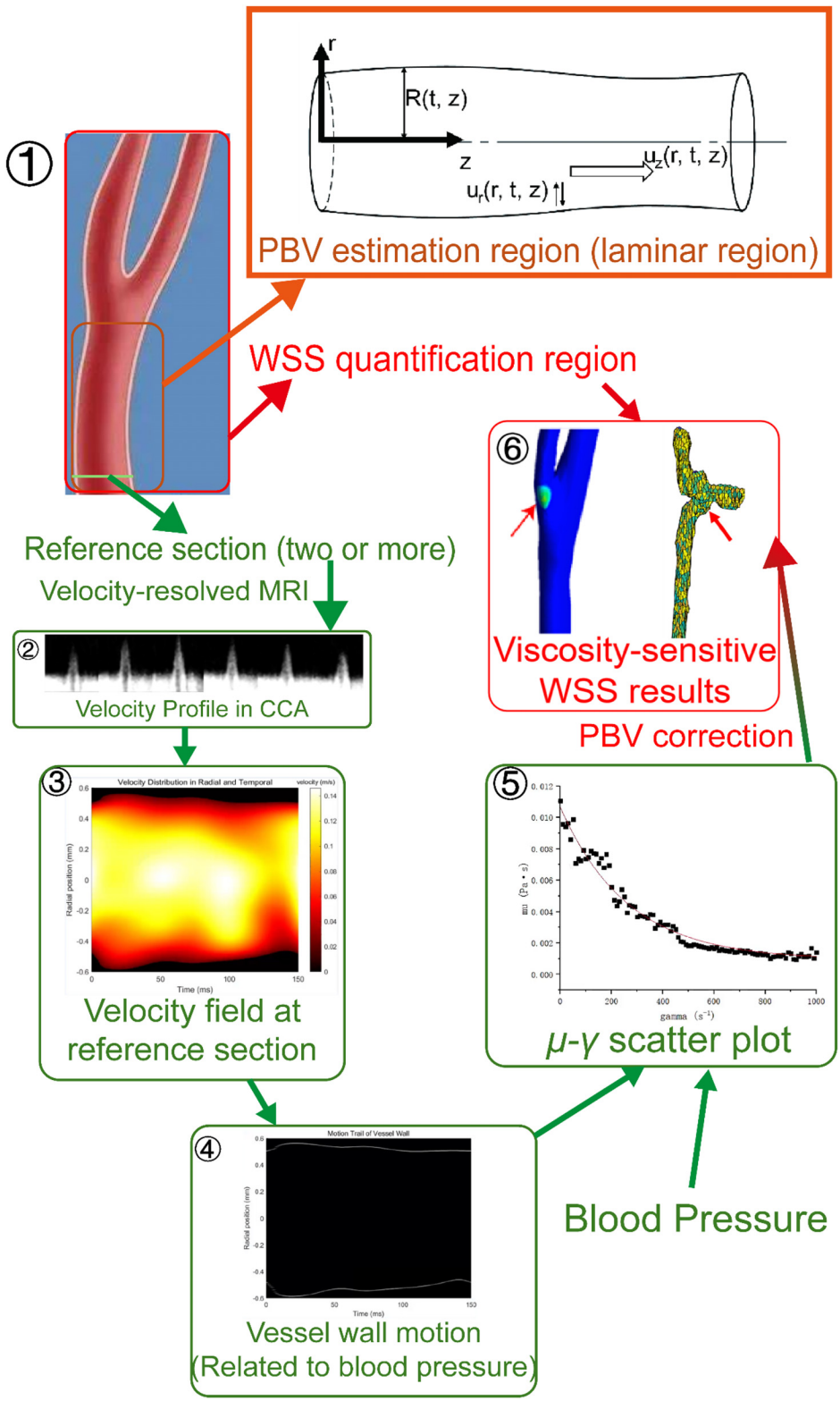

FIG. 1. Workflow of PBV estimation and correction for WSS quantification. PBV: personalized blood viscosity, WSS: wall shear stress.

divided into two groups: one with 15 rats (the HLP-rat group) and the other with 10 rats (the NC-rat group). The HLP-rat group was fed a high-fat diet (40% kcal fat, 1.25% cholesterol, 0.5% sodium cholate, and 0.2% 2-thiouracil) for 42 days. The NC-rat group was fed a conventional diet. MRI scans with an animal scanner were performed on Days 0, 10, 22, 31, and 42, and the blood pressure was measured by tail-cuff method with a pressure sensor during this period which has been used previously.[30] After the MRI scan on days 22, 31, and 42, a batch of rats (3 from the HLP-rat group and 2 from the NC-rat group) was sacrificed, and their left carotid arteries (LCA) were immediately harvested, then processed with H&E staining to prepare histological slices. In addition, on day 42, before euthanizing the rats, blood samples were collected from ten rats (5 from the HLP-rat group and 5 from the NC-rat group) for hemorheology testing.

A total of 23 male NZW rabbits, weighing 2.0–2.5 kg each, were maintained under a 12:12 light/dark cycle in humidity- and temperature-controlled rooms. After 7 days of adaptation, the rabbits were separated into the HLP-rabbit group and the NC-rabbit group, with 14 rabbits in the HLP-rabbit group fed a high-fat diet (10% kcal fat and 2% cholesterol) and nine rabbits in the NC-rabbit group fed a conventional diet. MRI scans were performed at week 0, 4, and 7, and the blood pressure was measured by animal blood pressure monitor (HHE Medical, Jinan) during this period. Four rabbits (3 from the HLP-rabbit group and 1 from the NC-rabbit group) were sacrificed after each scan session. The LCAs were immediately harvested and then processed with H&E staining. After each MRI scan, blood samples were collected from ten rabbits (5 from the HLP-rabbit group and 5 from the NC-rabbit group) for hemorheology testing.

C. Phantom test

To assess the accuracy of PBV estimation, a pulsating flow phantom driven by a peristaltic pump was designed. The structural design of the phantom is illustrated in Figs. 2(a) and 2(b). It comprises several components: a bottom plate (A), sealing side plates (B_1, B_2), interface side plates (C_1, C_2), a top plate (D), and a fluid pipeline (E). Plates A, B, and D are constructed from acrylic material, while C_1 and C_2 are fabricated using transparent 3D printing material. The fluid pipeline (E) consists of two glass tubes, each 210 mm in length and possessing an inner diameter of 7 mm, which is comparable to the CCA diameter of humans. To avoid the effect of shear rate fluctuation caused by pulsating flow on the results and to suppress the turbulent flow of the fluid, a 40% glycerol solution is used in this phantom. A capillary viscometer was used to measure the viscosity of the solution at 23.5 °C, and the result was (3.503 ± 0.029) mPa s (measurement details are described in supplementary material).

Before MRI scanning, the phantom was leveled and some silicone hosepipes were used to connect the phantom, peristaltic pump, and a storage bottle as Fig. 2(c). Then, the pump was turned on and the liquid levels in the tubes C_1 and C_2 were recorded to calculate the pressure gradient. During MRI scanning, a thermometer with 0.1 °C resolution monitored the temperature of the medium in the storage bottle and the temperature remained stable at 23.5 °C.

D. MRI protocols

For SD rats, MRI data were acquired using a Bruker Biospec 70/20 platform equipped with a 30 mm diameter surface coil operating

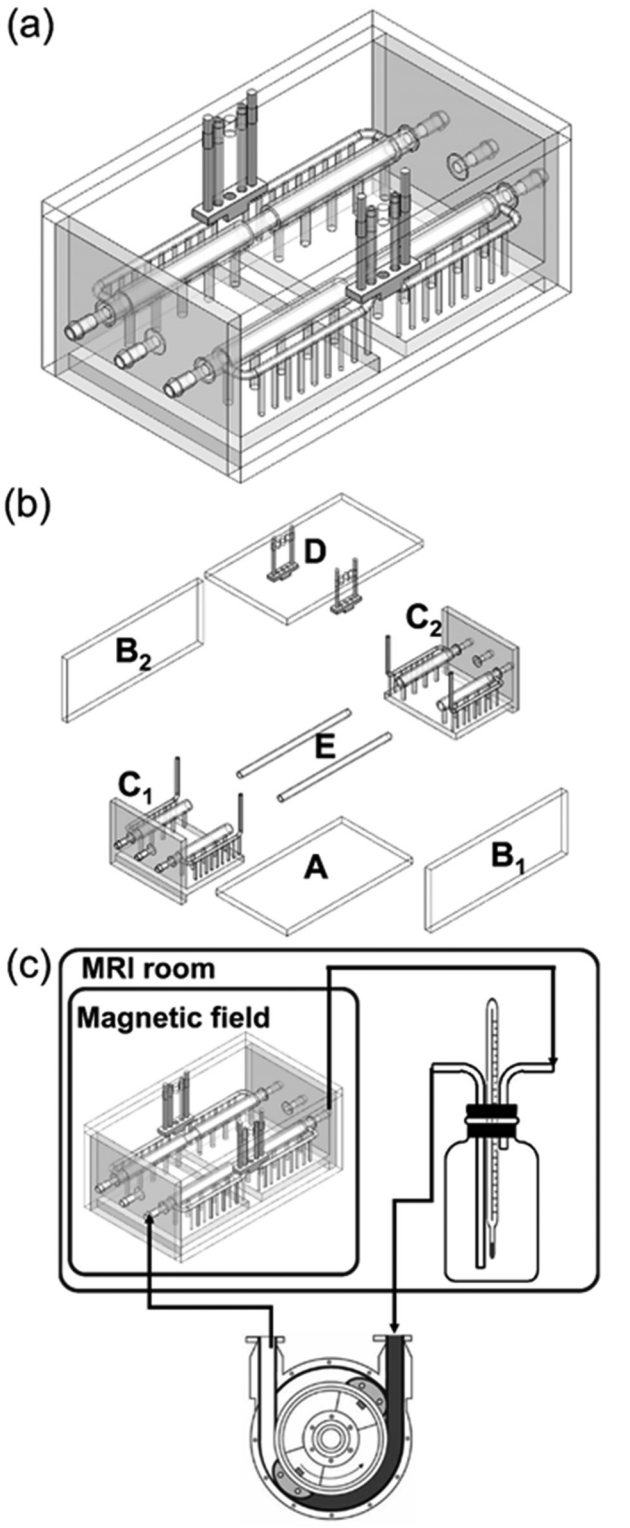

FIG. 2. Structure of phantom (a) for PBV accuracy assessment and its components (b). Schematic diagram of phantom connections and fluid direction (c). PBV: personalized blood viscosity.

at 7 Tesla (Bruker Biospin, Ettlingen). The imaging protocol employed a 2D time-of-flight (TOF) MRI sequence for the LCCA structural model and a pulse-triggered Local-saturation-and-delay imaging (LSDI) sequence for the velocity profile measurement at the inlet of LCCA. The LSDI sequence is an MRI sequence to observe blood flow velocity distribution by adding a perpendicular-to-CCA saturation pulse before the FLASH sequence, and the LSDI sequence was used in our previous studies to obtain blood flow velocity profile.[31] The 2D TOF MRA sequence parameters are as follows: field of view (FOV): $25.6 \times 25.6\,mm^2$, matrix: 160×160, in-plane resolution: $0.16 \times 0.16\,mm^2$, slice thickness: 1 mm, number of slices: 30, repetition time/echo time (TR/TE): 15/3.8 ms, flip angle (FA): 80°, number of excitations (NEX): 2. The pulse-triggered LSDI sequence parameters [with the local-saturate slice put on the slice 1 and slice 2 in Fig. 3(a)] are: FOV: $20 \times 15\,mm^2$, matrix: 128×96, in-plane resolution: $0.16 \times 0.16\,mm^2$, slice thickness: 2 mm, number of slices: 1, TR/TE: 100/2.9 ms, FA: 60°, NEX: 4. By altering the delay of the pulse trigger to divide the pulse cycle into six successive and equal parts, a series of dynamic LSDI results are achieved.

For NZW rabbits, MRI data were acquired using an uMR 780 MRI clinical platform with a 24-channel head and neck coil (United Imaging Healthcare Co., LTD, Shanghai) operating at 3 Tesla. The imaging protocol employed a 3D TOF MRA (tof3d_tra) sequence for the LCCA structural model and a 4D-Flow MRI (4Dflow) sequence for the velocity field data. The tof3d_tra sequence parameters are as follows: FOV: $100 \times 100 \times 80\,mm^3$, matrix: 256×256, number of slices: 80, in-plane resolution: $0.39 \times 0.39\,mm^2$ with a slice thickness of 1 mm, TR/TE: 18.4/4.2 ms, FA: 18°, NEX: 1. The 4Dflow sequence parameters are: FOV: $100 \times 100 \times 80\,mm^3$, matrix: 192×192, number of slices: 16, resulting in an in-plane resolution of approximately $0.52 \times 0.52\,mm^2$ with a slice thickness of 5 mm, TR/TE: 31.3/4.88 ms, FA: 9°, NEX: 1, and temporal resolution: 31.3 ms.

The phantom test was performed at 3T using the protocol same with rabbits. A synchronized virtual ECG waveform was used instead of the ECG trigger.

E. Efficiency of personalized blood viscosity correction in CFD prediction

For the laminar flow within an approximate circular tube, the non-Newtonian nature of its fluid viscosity usually corresponds to a specific velocity profile. This relationship stems from the definition of viscosity and implies that the closer the blood viscosity parameters match the actual viscosity, the fewer errors there will be in the velocity profile in comparison between CFD simulations and experimental results.

To verify the accuracy of the PBV-corrected CFD method, we designed an *in vivo* verification experiment following the protocol of Yi *et al.*[23] During the rats' MRI scanning on day 0, 3 rats in the NC-rat group were chosen randomly and performed CFD simulations to predict the velocity profiles at slice 1. Then, a quantitative comparison was performed to estimate errors of CFD results with PBV or empirical viscosity models.

F. Computational fluid dynamics (CFD) simulation

In ANSYS Fluent (version 2023R1, ANSYS Inc. Canonsburg, PA, USA) Solver, the pressure-based transient solver was chosen. The

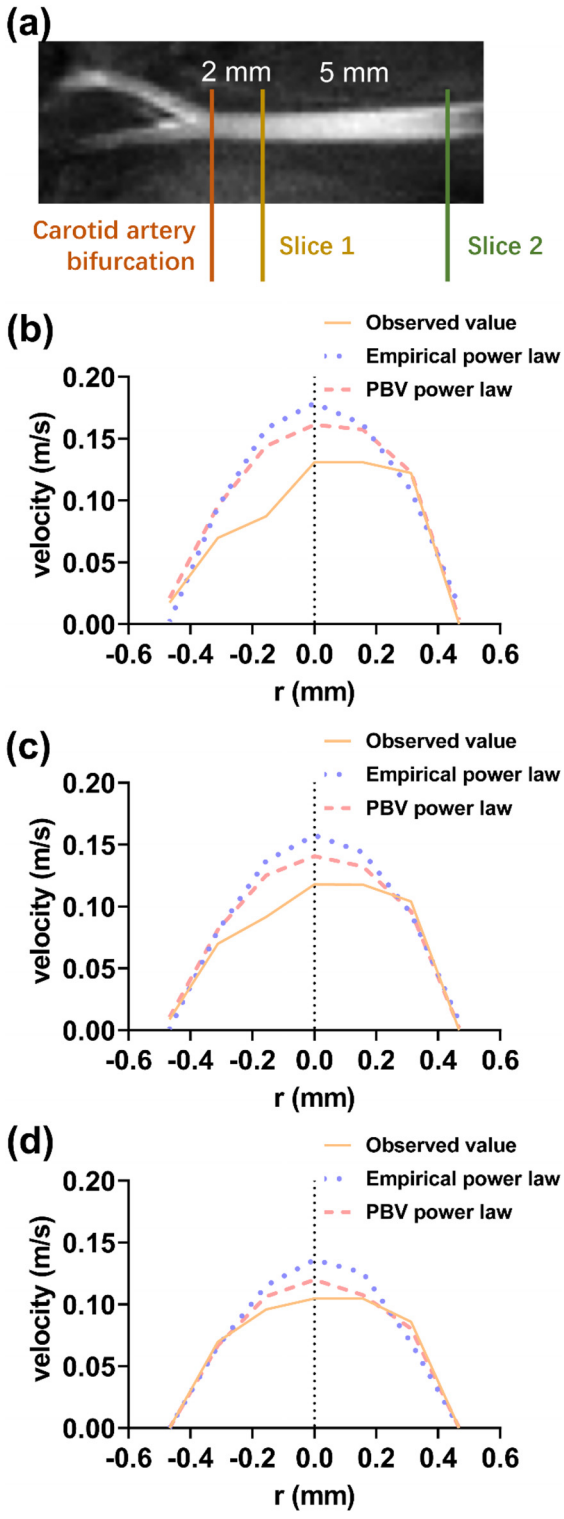

FIG. 3. The experimental illustration (a) and experimental results (b)–(d) of the flow velocity profile of the left common carotid artery in rats. r: radial distance from the center of the vessel.

vascular geometry was provided by the STL file reconstructed by TOF-MRA. In the fluid material settings, the density was assigned a value of 1050 kg/m^3 which has been used previously,[32,33] and the viscosity was input using the expression provided in Eq. (7) or (8) The models were prescribed with a laminar flow based on the Reynolds number calculated for each geometry (Table S1). The iterative process terminates when the residuals for continuity, x-velocity, y-velocity, and z-velocity are all less than 0.001.

To define the inlet boundary at the left common carotid artery (LCCA), the velocity profiles derived from MRI were bicubically interpolated to a resolution of 1 μm × 1 ms in both radial and temporal dimensions. Then, the mass flow rate at the inlet can be calculated by the integration of velocity in the LCCA inlet section and input into the inlet boundary conditions by Fourier Decomposition. The outlet at the left external carotid artery and left internal carotid artery were set as the outflow boundary, and the lateral wall of vascular was set as the no-slip wall boundary.

G. Computation of time-averaged wall shear stress (TAWSS) and oscillatory shear index (OSI)

The time-averaged wall shear stress (TAWSS) and oscillatory shear index (OSI) represent the intensity and directional change of the WSS vector from a predominant blood flow direction during the cardiac cycle and are defined by

$$TAWSS = \frac{1}{T}\int_0^T \tau_w(t)dt, \tag{9}$$

$$OSI = \frac{1}{2}\left(1 - \frac{\left|\int_0^T \vec{\tau}_w(t)dt\right|}{\int_0^T \left|\vec{\tau}_w(t)\right|dt}\right), \tag{10}$$

where τ_w is the WSS vector as defined in Eq. (11).

$$WSS = \tau_w(t) = \mu \cdot WSR = \mu\left(\frac{du_z(t)}{dn}\right)_{r=R}, \tag{11}$$

where n is the normal vector of vascular endothelium.

H. Statistical analysis

In this study, statistical analyses were conducted to examine the performance of the PBV estimation, as well as highlight the importance of personalized and non-Newtonian blood viscosity in the hemodynamic analysis and early diagnosis of the AS. All statistical tests were performed using GraphPad Prism 9, and the significance level was set at $p = 0.05$.

Measured and calculated hemodynamic variables and test results are presented as mean ± SD. T-test was used to compare healthy vs high-fat-fed groups. Pearson correlation is used to analyze the relationship between test results and personalized blood viscosity. A repeated measures ANOVA with Greenhouse-Geisser correction (for non-sphericity) was performed to assess the effect of PBV correction. Post-hoc pairwise comparisons used Tukey's HSD test to control family wise error rates. Effect sizes (f calculated by partial η^2) and p-values are reported.

The sample size was determined by power analysis using G*power 3.1.9.7. Based on preliminary data from a pilot study ($n = 5$ per group), we estimated a large effect size (Cohen's $d = 2.5$ for TAWSS difference between HLP and NC groups) with $\alpha = 0.05$ and power = 0.8. The analysis indicated a requirement of four animals per group. To account for variability and attrition, we expanded to 15 HLP rats,10 NC rats, 14 HLP rabbits, and 9 NC rabbits.

III. RESULTS

A. Phantom results of PBV estimation

The PBV estimation can measure the viscosity of the flowing medium which in pulsating tube flow as accurately as capillary viscometers.

The dynamical liquid level difference between C_1 and C_2 tubes is shown in Figs. 4(a) and 5 (Multimedia view). The pressure difference between the inlet and outlet is given by the product of the liquid level difference, medium density, and gravitational acceleration ($g = 9.8$ m/s^2). The medium temperature is kept at 23.5 °C.

Sagittal TOF-MRA image and axial 4D-Flow MRI result are shown in Figs. 4(b) and 4(c), along with the μ-γ scatterplot [Fig. 4(d)], A 40% glycerol solution is a Newtonian fluid with a viscosity value $\mu = 3.497$ mPa s, differing by less than 0.2% from viscometer measurements (3.503 ± 0.029 mPa s).

B. Velocity profile for rats

PBV correction improves the alignment of CFD-predicted velocity profiles with actual measurements.

Figures 3(b)–3(d) show the velocity profiles for three healthy rats at Slice 1 in Fig. 3(a). Solid lines are ground truth obtained by LSDI, dashed lines are CFD results with PBV correction, and dotted lines are CFD results with empirical power-law blood viscosity. Table I lists area-weighted root mean square errors. The results show that PBV correction reduces CFD errors by 11%–23% and aligns better with actual blood flow in rats' LCCA compared to empirical power-law fluid models.

C. Blood lipid levels of rats and rabbits

After long-term high-fat feeding, the rats and rabbits had significantly higher levels of blood lipids (especially LDL-C, the low-density lipoprotein cholesterol that is one of the components of atherosclerotic plaque).

The blood lipid levels of rats on day 42 are shown in Fig. S1(a). The total cholesterol (TC, $p < 0.01$) and low-density lipoprotein (LDL-C, $p < 0.01$) levels in the HLP-rat group were significantly higher than those in the NC-rat group, indicating that hypercholesterolemia had developed in the HLP-rat group. The blood lipid levels of the rabbits are shown in Fig. S1(b) at week 4. All indicators for the HLP-rabbit group were significantly higher than those for the NC-rabbit group at week 4 (TC, $p < 0.01$, TG, $p < 0.05$, HDL-C, $p < 0.05$, and LDL-C, $p < 0.01$), indicating that the HLP-rabbit rabbits had developed combined hyperlipidemia.

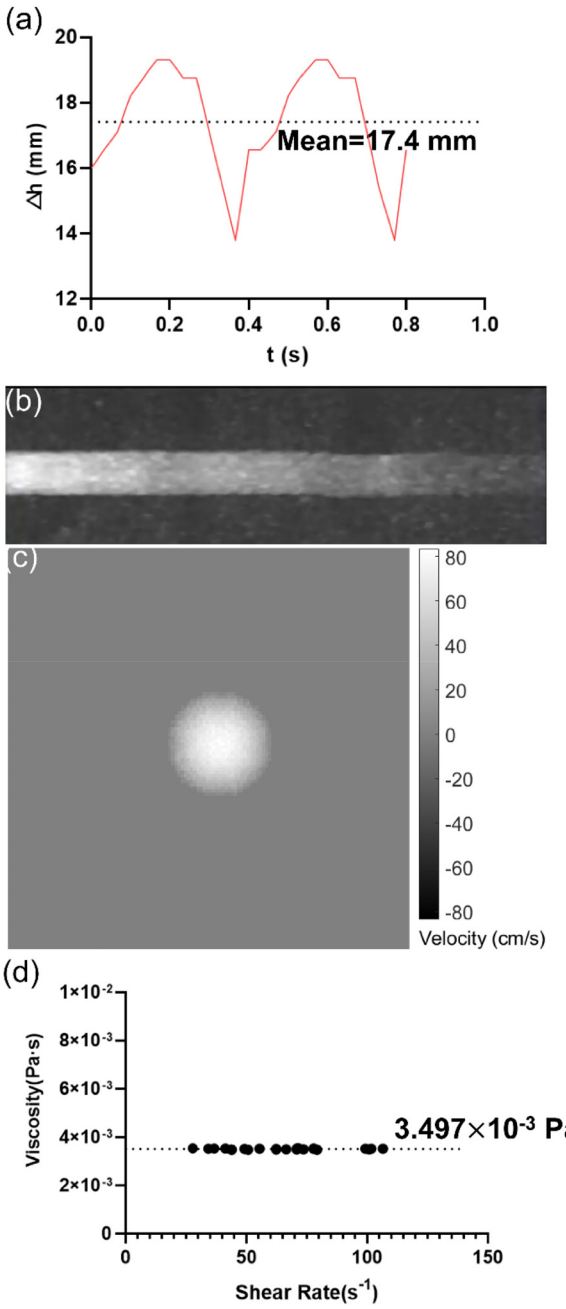

FIG. 4. Typical results of phantom experiment. (a) shows the pressure difference between inlet and outlet of the phantom during MRI scanning. The sagittal TOF-MRA image and axial velocity maps obtained by 4D-Flow MRI are shown in (b) and (c), and the personalized blood viscosity (PBV) estimation evaluated μ-γ scatterplot is shown in (d).

D. Wall shear stress (WSS) results of rats and rabbits with and without PBV correction

The Reynolds number (Re) in the LCCA of HLP and NC rats were not more than 2000 (Table S1), which means it is appropriate to identify the blood flow of the left carotid artery as laminar flow. Based on this premise, the WSS results with PBV correction were equipped with viscosity-sensitive features, which can detect WSS abnormal regions earlier than those results with empirical blood viscosity.

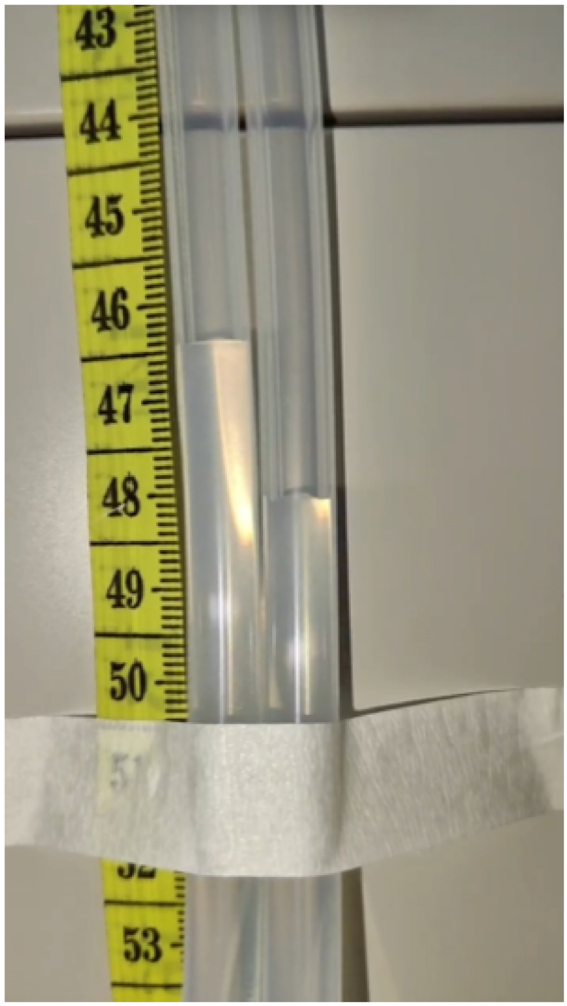

FIG. 5. The height difference of liquid level between the inlet C_1 (the left silicon tube) and outlet C_2 (the right silicon tube) on the phantom (unit: centimeter). Multimedia available online.

Figure 6 shows typical TAWSS results in rats. The three columns on the left represent the changes in TAWSS maps of three rats in the HLP-rat group over the high-fat feeding period. The fourth column displays the TAWSS maps of rats in the NC-rat group. All these maps employed the PBV results as their viscosity models. Furthermore, the fifth column presents the TAWSS results for the same case featured in the second column but with an empirical power-law fluid model used. The corresponding OSI results are shown in Fig. S2, which only shows an abnormality on day 42.

The results of CFD-MRI using PBV correction indicated that TAWSS abnormalities were presented in the LCCA of high-fat-fed rats on day 31. However, the CFD results using the empirical power-law fluid model showed abnormal TAWSS positivity only on day 42. The changes in the minimum TAWSS (HLP-rat group: 0.62 ± 0.13 Pa vs

TABLE I. The area-weighted quantify results of root mean square-errors with the PBV and empirical power-law viscosity.

Figure No	RMSE with PBV	RMSE with empirical power-law viscosity
Fig. 3(b)	2.43%	3.15%
Fig. 3(c)	1.40%	1.96%
Fig. 3(d)	0.89%	1.00%

NC-rat group: 1.00 ± 0.15 Pa, $p < 0.05$ at day 31) and maximum OSI (HLP-rat group: 0.12 ± 0.06 vs NC-rat group: 0.03 ± 0.02 Pa, $p < 0.05$ at day 42) values during the feeding period (Fig. S3) revealed significant intergroup differences between HLP-rat and NC-rat groups.

Figure 7 demonstrates H&E-stained histological outcomes on day 31, with panels (b) and (d) displaying magnified views of red-boxed regions from (a) and (c) respectively. Histopathological analysis reveals marked endothelial thickening in left carotid arteries, characteristic of low WSS-induced vascular remodeling. This morphological alteration correlates with TAWSS reduction quantified by PBV-corrected CFD-MRI (Fig. S4, HLP-rat group: 0.62 ± 0.13 Pa vs NC-rat group: 1.00 ± 0.15 Pa, $p < 0.05$). Notably, empirical viscosity assumptions yield non-significant intergroup differences (HLP-rat group: 0.79 ± 0.15 Pa vs NC-rat group: 0.83 ± 0.16 Pa, $p = 0.77$). The PBV-corrected WSS results successfully highlight pre-stenotic hemodynamic abnormalities preceding structural changes.

Figures 8 and S5 show typical TAWSS results obtained from 4D-Flow MRI in rabbits. Before modeling, both the TAWSS results using PBV and empirical models were similar and within a healthy range. At week 4, there was a difference in results between the two methods. This difference was concentrated in the individuals of the HLP-rabbit group, specifically manifested as a significant enlarge in low WSS region using PBV compared to that with the empirical power law model (PBV: HLP-rabbit = 66.6% ± 2.8%, NC-rabbit = 29.6% ± 15.0%, $p < 0.05$, empirical model: HLP-rabbit = 45.6% ± 2.6%, NC-rabbit = 33.4% ± 9.2%, $p = 0.07$). This difference diminished at week 7. Figures S6 and S7 show the typical H&E-staining sections of the LCA from two groups of rabbits at week 4 and 7. At week 4, the sections showed a small-scale smooth muscle proliferation. The observed changes expanded at week 7, with inflammation and foam cell aggregation appearing, indicating that plaques were beginning to form.

Figure S8 shows the typical results of 3D TOF-MRA of rabbit carotid artery. At week 7, the LCCA diameters of the rabbits in the HLP-rabbit group (2.15 ± 0.30 mm) are significantly lower than those in the NC-rabbit group (2.67 ± 0.36 mm, Fig. S9), and the signal of the left internal carotid artery is weak, indicating arteriostenosis occurred currently.

Post-hoc power analysis confirmed that the actual sample sizes provided ≥ 80% power for the differences in all of the parameters in the present study (Table S2).

E. Personalized blood viscosity results of rats and rabbits

PBV estimation enhances the accuracy of WSS results by dynamically accounting for viscosity variations.

The changes in blood viscosity of SD rats measured using the PBV estimation are shown in Figs. 9(a) and 9(b). The HLP-rat group showed a significant increase in low-shear viscosity on day 31. On day 42, due to increased viscosity-related resistance, there are no regions that maintain a shear rate above 800 s^{-1}. In contrast, there was no significant change in blood viscosity in the NC-rat group during the same period. Figures 9(c)–9(e) show the changes in blood viscosity during weeks 0, 4, and 7 of high-fat feeding in NZW rabbits. The results suggest that there is a continuous downward trend in low-shear blood viscosity within the HLP-rabbit group.

Figures 9(f)–9(j) demonstrate the correlation between the PBV results and the measurements obtained using the clinical blood rheometer. There is a strong correlation (r and p values are put in the figures, respectively) between the results obtained from both methods in various shear rates, regardless of whether the blood samples are from rats or rabbits.

IV. DISCUSSION

We have proposed a novel numerical method to estimate non-Newtonian blood viscosity *in vivo* from MRI data, and correct WSS in hemodynamic analysis. The proposed method has distinctive advantages over empirical parameters. Specifically, it accounts for blood viscosity alterations induced by hyperlipidemia. This method can also be applied across species.

A. Blood viscosity-sensitive WSS results can highlight endothelial injury region before fat deposition

Current clinical imaging modalities (e.g., carotid ultrasound or MRI) primarily focus on detecting structural abnormalities (e.g., plaque thickness or stenosis), manifesting mainly the symptoms after endothelial injury and lipid accumulation. In contrast, PBV-corrected WSS mapping enables noninvasive identification of hemodynamic risk markers (e.g., low TAWSS) before morphological changes occur. This capability could be used to transform early atherosclerosis screening in patients by shifting the diagnostic paradigm from geometric to functional hemodynamic assessment, thereby enabling timely interventions (e.g., lipid-lowering therapies or viscosity regulation) to prevent irreversible vascular damage.

Wall shear rate (WSR) and blood viscosity are the two factors of wall shear stress (WSS). However, the important effect of blood viscosity has been overlooked in previous studies. These studies suggest that the vessels that are occupied by heavy atherosclerosis, the blood flow streamlines were dramatically changed which makes the blood viscosity effect negligible on WSS.[20,21] But it does not mean that WSS is ineffective before fat deposition. The destruction of healthy endothelium by abnormal WSS has been demonstrated in microfluidic devices *in vitro*.[34,35]

In the present study, a PBV estimation method with the power-law model was used to measure blood viscosity *in vivo*. Previous studies have proved that the blood viscosity differences among various shear-thinning non-Newtonian fluid models (e.g., Carreau, power-law, Herschel–Bulkley, and Quemada) under physiological shear rate (1–1000 s^{-1}) are not enough to cause obvious changes in the TAWSS map.[28,29] Therefore, in this study, power-law expression with low complexity and no input of other physiological parameters such as hematocrit was used to fit the discrete blood viscosity scatters.

As shown in Fig. 6, the PBV-corrected rather than empirical-viscosity-applied TAWSS map signed low WSS regions on day 31.

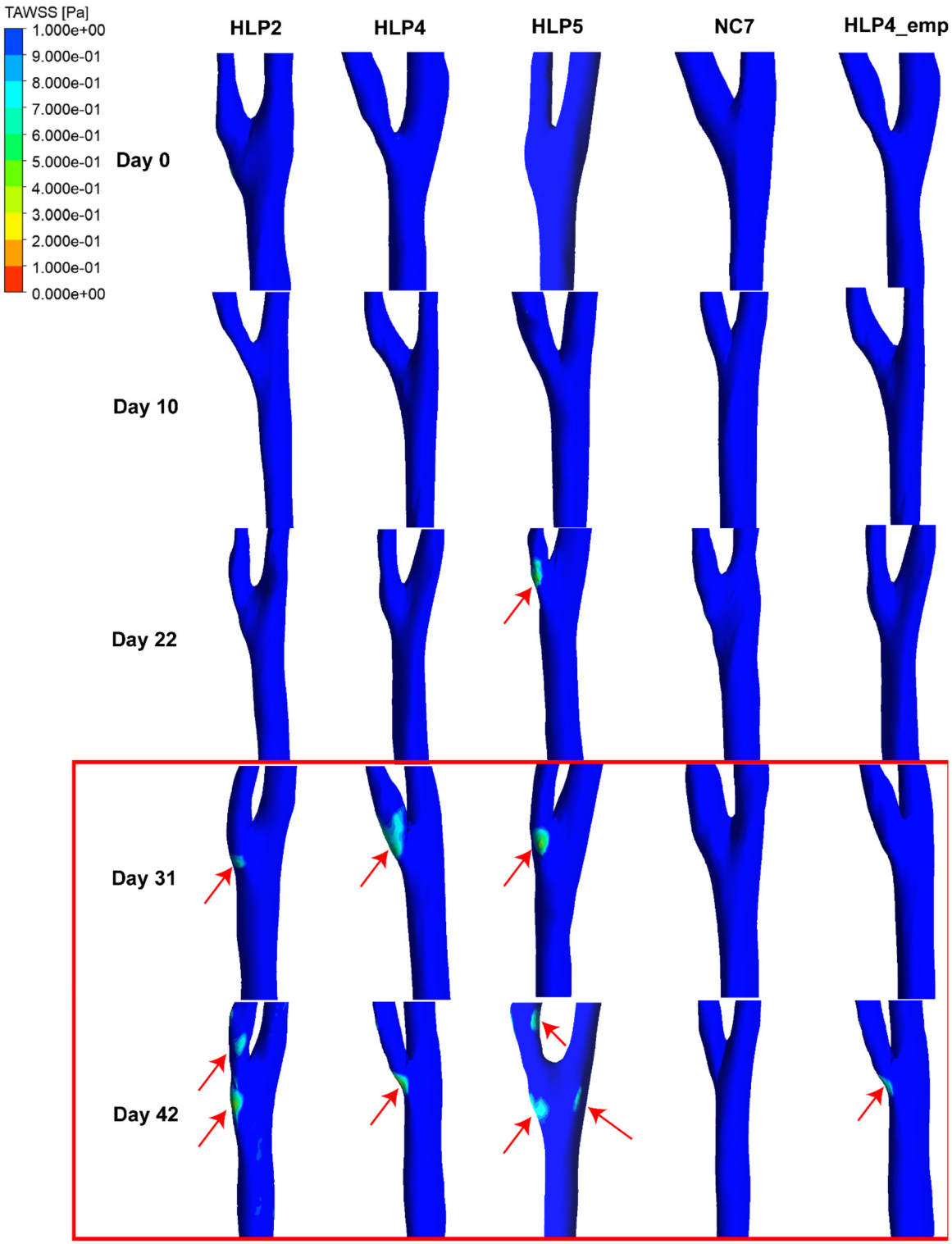

FIG. 6. The typical TAWSS results of rats are demonstrated. HLP2, HLP4, and HLP5 are three series of TAWSS maps from the HLP-rat group, while the maps in NC7 column are from NC-rat group. The HLP4_emp column shows TAWSS results using the empirical power-law blood viscosity model. Low TAWSS regions are marked with red arrows. TAWSS: time-averaged wall shear stress.

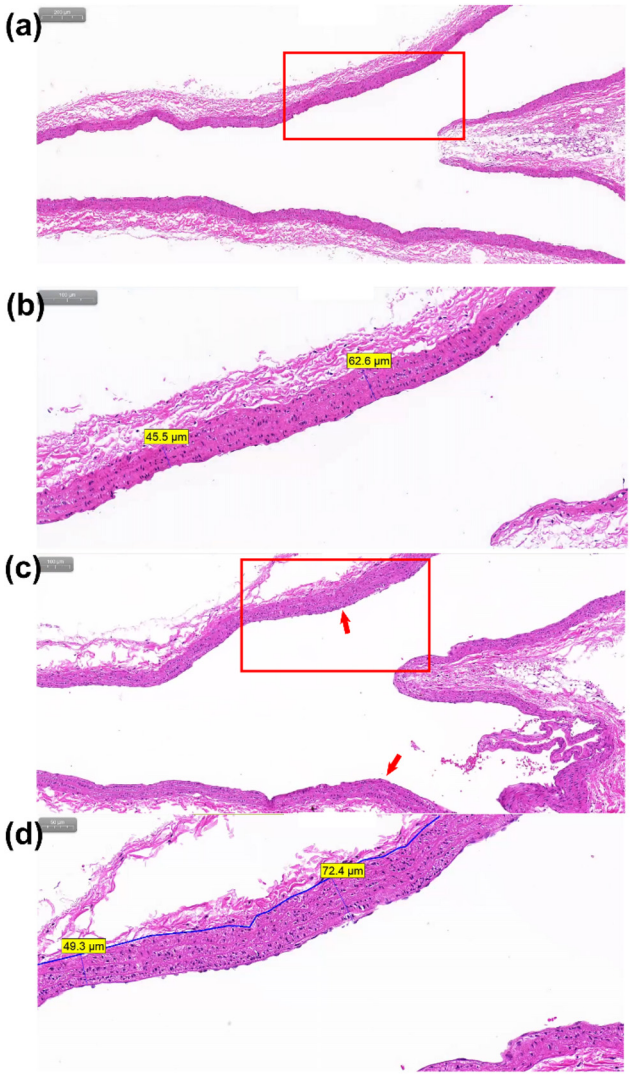

FIG. 7. Typical H&E-stained sections (a) and magnified images (b) of the rat in NC-rat group on day 31. Corresponding sections (c) and magnified images (d) of the rat in HLP-rat group. Endothelial injury lesions are marked with red arrows.

On the other hand, the endothelial cells in hyperlipidemia rats' CCA bifurcation underwent a focal and obvious morphological change. For the hyperlipidemia rats, the thickness of lesional endothelium is thicker than healthy endothelium [Figs. 7(b) and 7(d)], but no foam cells were observed. These results indicate that viscosity-sensitive WSS results are sensitive enough to highlight the endothelium lesion at an earlier stage which is anterior to fat deposition.

In addition, the positive effect of PBV correction has been quantified by TAWSS evolution (Figs. S3 and S4) and three-way repeated measure ANOVA (Table II). The significance of Diet ($p < 0.01$) means that there is a significant $TAWSS_{min}$ difference caused by feed type, and the significance of Diet×PBV ($p < 0.05$) means that PBV correction is beneficial with screening high AS risk subjects caused by blood viscosity abnormality. Similar results were found in rabbits' experiments (Table III), but the low WSS level significances were much higher. In addition to the different indicator effects, the faster hyperlipidemia disease progression in rabbits is also a main reason.[36,37]

The difference in blood viscosity between empirical viscosity and PBV results led to the difference in secondary flow pattern, especially in regions with enhanced convection such as vessel branching, which may be the main reason for the increase in OSI map difference and the sharp increase in OSI_{max} square difference in HLP-rat group on the day 42. This phenomenon has been discovered before in previous studies.[38] However, due to spatial resolution limitations, the MRI method used in the present study was not able to capture the weak secondary flow changes in the carotid arteries of the small experimental animals in the experiment. It is necessary to verify the accuracy of the OSI results in larger animals or humans, which will be confirmed in our future studies.

B. Robustness of PBV estimation across different species and pipe diameters

The non-Newtonian property of blood is a macroscopic manifestation of the mechanical properties of red blood cells.[39] The velocity distribution of blood flow is affected by the lumen size.[40,41] Therefore, it is necessary to evaluate the robustness of PBV estimation in vessels with various inner diameters.

In the present work, rats and rabbits were used to evaluate the robustness of this solver with different CCA diameters. Comparing the results of PBV and hemorheological tests in both rats and rabbits, they were strongly correlated [Figs. 9(f)–9(j)]. Additionally, the viscosity of blood-like Newtonian fluid (used in Ref. 42) may be measured accurately by this method.

The interindividual variability in hemodynamic responses to blood viscosity and vascular geometry may significantly influence the progression of atherosclerosis. Our results demonstrated divergent viscosity trends between rats and rabbits under high-fat diets (Fig. 9), likely attributable to species-specific differences in hematocrit and red blood cell mechanics (Fig. S10). Red blood cell aggregation under low shear rate is the main cause of increased blood viscosity. For the hyperlipidemia rabbits, high-fat diet-induced low hematocrit suppressed red blood cell aggregation which has been reported by previous study.[43] The underlying cause is not clear.

Variations in hematocrit, red blood cell mechanics, and blood composition highlight the necessity of personalized viscosity modeling. The PBV framework accounts for these interindividual differences by incorporating *in vivo* velocity profiles and pressure dynamics, thereby enabling patient-specific identification of hemodynamically vulnerable regions. Future studies should quantify the contribution of genetic, metabolic, and anatomical factors to interindividual variability in WSS-viscosity interactions.

C. Compatibility of PBV estimation in computational fluid dynamics (CFD) and 4D-flow MRI

Due to the different clinical application scenarios of CFD and 4D-flow MRI, it is of vital importance to ensure the compatibility of PBV estimation with both of them. Blood flow patterns (laminar/turbulent) significantly influence WSS quantification in hemodynamic analysis, especially in CFD-derived measurements. 4D-flow

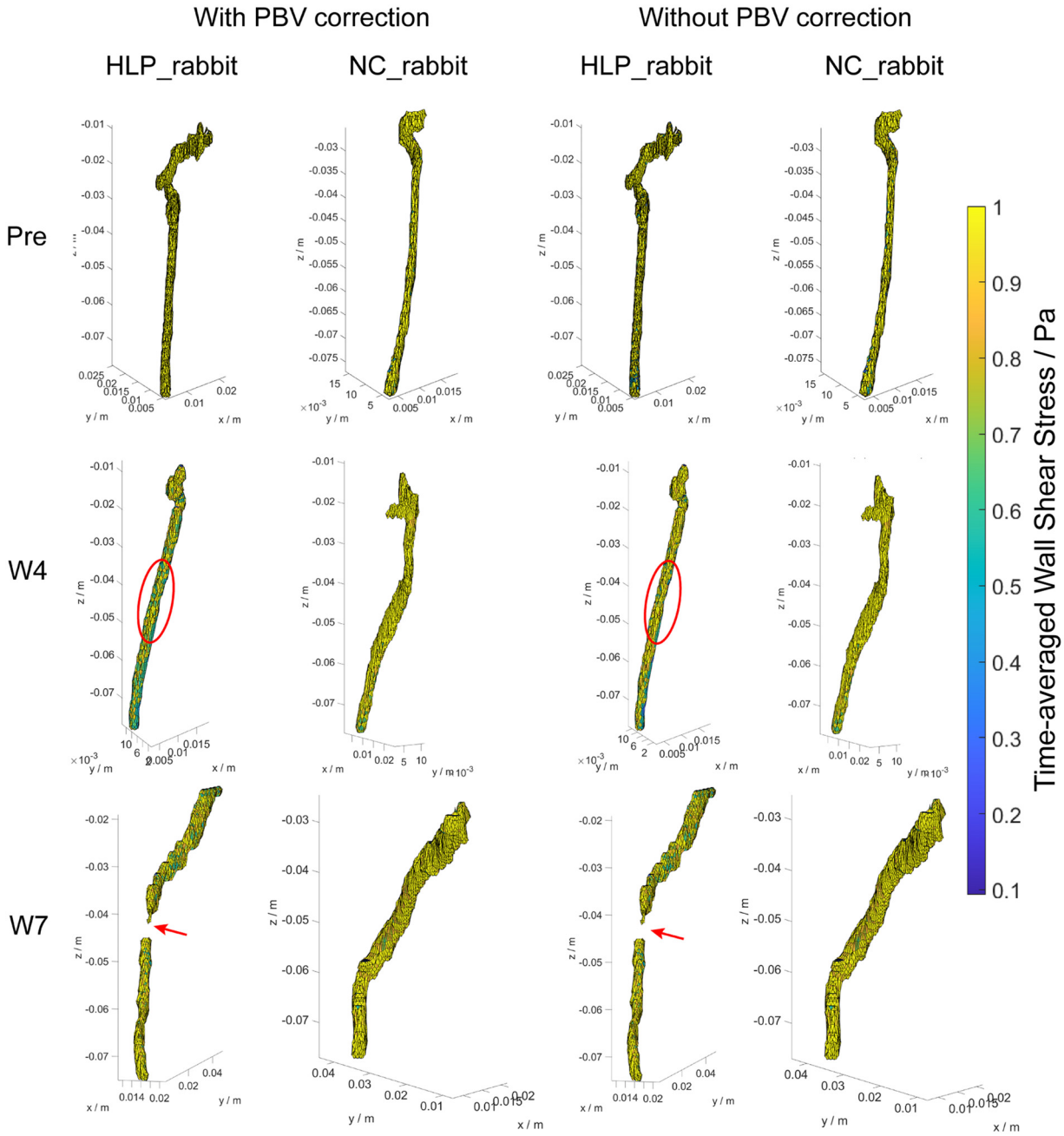

FIG. 8. Typical TAWSS maps of the left common carotid arteries in healthy rabbits and rabbits with hyperlipidemia, with and without correction of the PBV estimation. The red ellipses marks difference between the time-averaged wall shear stress results with and without PBV correction. The red arrows marks the arterial stenosis regions. HLP: hyperlipidemia, NC: negative control, PBV: personalized blood viscosity, Pre: before high-fat diet period, W4: the 4th week of high-fat diet period, W7: the 7th week of high-fat diet period.

MRI enables direct *in vivo* visualization of three-dimensional blood flow patterns and provides critical physiological data needed in PBV-model analysis through noninvasive velocity mapping.[44] CFD simulations offer predictive flexibility by modifying vascular geometry and boundary conditions. Postoperative hemodynamic changes can be evaluated using CFD approaches.[45] The dual-modality compatibility may improve clinical decision-making for both diagnostic evaluation and surgical planning. For instance, in patients with asymptomatic hyperlipidemia, PBV-corrected WSS maps could localize low WSS regions and guide personalized therapeutic strategies (e.g., PCSK9

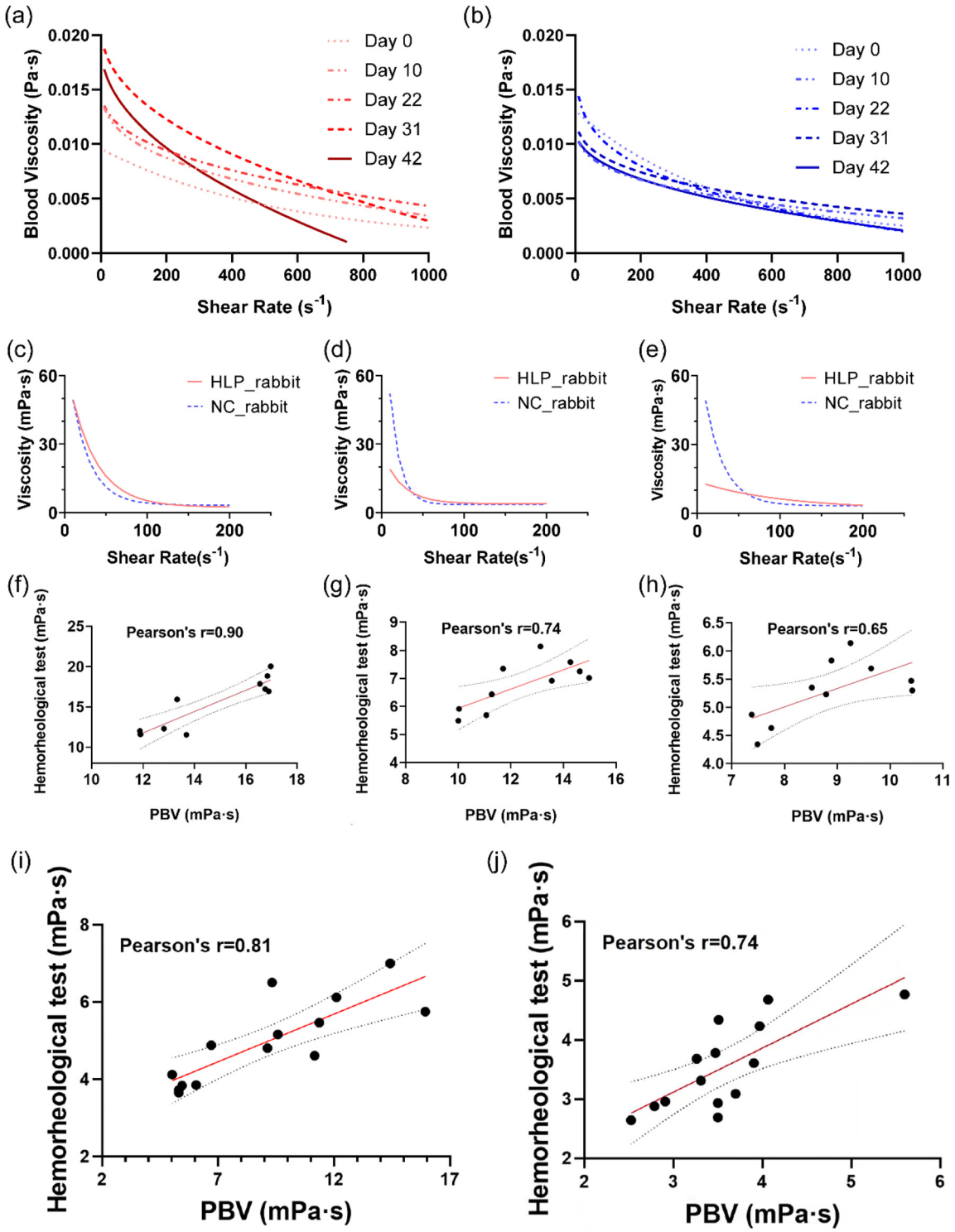

FIG. 9. Changes in blood viscosity were examined in hyperlipidemic rats (a) and healthy rats (b) at different feeding times. Blood viscosity was measured in hyperlipidemic and healthy rabbits at pre-feeding (c), week 4 (d), and week 7 (e). Blood viscosities of rats obtained from PBV estimation and hemorheological tests in low shear rate [(f) $p < 0.001$], middle shear rate [(g) $p < 0.05$], and high shear rate (h, $p < 0.05$). Blood viscosities in rabbits obtained from PBV estimation and hemorheological tests in middle shear rate [(i) $p < 0.001$] and high shear rate [(j) $p < 0.01$]. PBV: personalized blood viscosity.

TABLE II. Repeated measure ANOVA results for rats' $TAWSS_{min}$ values.[a]

	F	p
① Day	0.28	0.89
② Diet	10.80	<0.01
③ With/without PBV	1.00	0.33
① × ②	3.66	<0.01
① × ③	0.49	0.74
② × ③	6.79	<0.05
① × ② × ③	0.64	0.64

[a]Post-hoc comparisons were corrected using Tukey's HSD test.

TABLE III. Repeated measure ANOVA results for rabbits' low WSS level.[a]

	F	p
① Week	57.64	<0.0001
② Diet	28.96	<0.0001
③ With/without PBV	5.88	<0.05
① × ②	11.51	<0.0001
① × ③	2.09	0.11
② × ③	11.64	<0.01
① × ② × ③	3.25	<0.05

[a]Post-hoc comparisons were corrected using Tukey's HSD test.

inhibitors to mitigate endothelial dysfunction or alter the shape with stents).

Our experimental validation result confirms PBV estimation's compatibility with CFD and 4D-flow MRI for quantifying WSS in carotid arteries. For individuals with hyperlipidemia, PBV correction makes the WSS results obtained by the two methods better relative to the empirical viscosity, as reflected in their better matching with histological findings. The results showed that the viscosity obtained by PBV was better consistent with the actual physiological viscosity.

D. The computational fluid dynamics (CFD) simulation can yield more reliable wall shear rate (WSR) results after correction with PBV estimation

The inhomogeneous concentration of red blood cells within blood flow is the main cause of the non-Newtonian viscosity nature.[39,40] Therefore, blood viscosity information obtained *in situ* is more reliable than empirical viscosity parameters. Yi *et al.* corrected CFD data using a series of *in-vitro*, individually measured non-Newtonian blood viscosity curves.[23] However, there are some deviations of WSR between the CFD results and *in vitro* particle image velocimetry results in the flow velocity profiles. In addition to the PIV measurement errors mentioned in Ref. 23, there is also a difference in red blood cell distribution between Couette flow in cone-plate viscometry and Poiseuille flow in arteries.[46]

In the present study, the results of the PBV estimation were validated by using a similar experimental protocol. By comparing the CFD-predicted flow velocity profiles with the actual observed ones, it is demonstrated that the proposed method can more accurately examine the microscopic stress–strain relationship in fluid systems, and the WSR results become more reliable (Fig. 3 and Table I, the area-weighted root mean square error of velocity field is less than 2.5% with PBV correction, which is the 80% of the error value without PBV correction).

E. The relationship between the PBV-corrected 4D-Flow MRI results and subsequent vascular diameter changes

Previous studies have demonstrated the existence of a negative feedback mechanism involving WSS, nitric oxide (NO) release, and vascular diameter.[47,48] Specifically, an increase in WSS triggers a greater release of NO, which in turn stimulates vascular and thereby further elevation of WSS is inhibited. Conversely, a decrease in WSS leads to reduced NO release, ultimately resulting in smooth muscle proliferation that narrows the vascular lumen.

Such a phenomenon was also observed in the present study. Before significant stenosis in TOF-MRA images of the HLP-rabbit group was observed at week 7, we detected a decline in the overall TAWSS levels within the vessels at week 4 using PBV-corrected results. This result may indirectly and qualitatively reflect the accuracy and reliability of TAWSS values derived from the PBV estimation.

F. Relationships between blood lipid levels and blood viscosity/wall shear stress parameters

Clinical studies revealed moderate positive correlations between blood viscosity and lipid parameters.[49] However, blood lipid levels are not a dominant factor in blood viscosity variance in subjects. This correlation is not always true in rabbit models with fed high-fat diets.[43] Lipoprotein apheresis treatment reduced whole blood viscosity, red blood cell aggregation, and deformability. These hemorheological improvements may contribute to reduced atherosclerotic risk.[50]

Unlike blood viscosity, lipid levels exhibit non-linear relationships with WSS magnitude. This complexity arises from viscosity coupling with wall shear rate in WSS calculations.[18] Our results suggest that both increased and decreased blood viscosity may induce low WSS regions, which is consistent with previous conclusions.[51] Therefore, it is necessary to accurately quantify and monitor WSS before and after regulating blood viscosity.

G. Interindividual variability in WSS and blood viscosity effects

Interindividual variability in WSS responses may arise from genetic polymorphisms (e.g., APOE $\varepsilon 4$ allele affecting lipid metabolism) and metabolic factors (e.g., hyperglycemia-induced red blood cell aggregation).[52,53] Future studies should integrate multi-omics data to refine PBV models.

Furthermore, within the same species, variations in vascular curvature, lumen diameter, and baseline lipid profiles could modulate the coupling between blood viscosity and WSS. The observed interindividual differences in hemodynamic responses to blood viscosity and WSS underscore the importance of personalized modeling in atherosclerosis risk assessment. Even within homogeneous experimental groups (e.g., HLP-rat group), PBV-corrected TAWSS maps revealed substantial variations in low WSS regions (Fig. 6). This observation suggests that

intrinsic biological variability, in addition to diet-induced hyperlipidemia, modulates the interplay between WSS and blood viscosity. Such variability may arise from multiple sources: (1) variations in vascular curvature, lumen diameter, and bifurcation geometry across individuals inherently alter local flow patterns, thereby modifying WSS distribution independently of viscosity.[54] (2) Interindividual differences in hematocrit, red blood cell aggregation, and deformability directly influence non-Newtonian blood viscosity.[31,55,56] Our PBV framework dynamically captures these variations through *in vivo* velocity profiling and MRI geometric measurement, as evidenced by the strong correlation between PBV-estimated and rheometer-measured viscosity across shear rates [Figs. 9(f)–9(j)].

These findings align with the emerging evidence that individualized WSS quantification (rather than the traditional methods with empirical parameters) are critical for predicting plaque formation. The PBV method's ability to resolve interindividual differences in both rats and rabbits (Fig. 9) highlights its translational potential for human studies, where genetic, anatomic, and metabolic diversity is far greater. Future integration of multi-omics data (e.g., genomic and proteomic) with PBV-corrected hemodynamic models could further stratify patients based on their unique "hemodynamic fingerprint," enabling precision prevention strategies tailored to individual risk profiles.

H. Genetic and metabolic modulators of WSS–atherosclerosis interaction

Beyond hemodynamic and rheological factors, genetic and metabolic variations may profoundly influence the relationship between WSS and endothelial dysfunction in atherosclerosis. Epigenetic regulation factors in mechanosensitive pathways, such as Aβ-induced Piezo1 inhibition and eNOS phosphorylation, could alter endothelial responsiveness to WSS magnitudes, potentially explaining interindividual differences in plaque localization despite similar hemodynamic profiles.[57–59] For instance, gene polymorphisms of eNOS such as T786C and G894T have been related to cardiovascular diseases.[60] Similarly, metabolic disorders like diabetes mellitus may exacerbate WSS anomalies through dual mechanisms: (1) hyperglycemia-induced glycation of plasma proteins elevates blood viscosity, and (2) oxidative stress impairs endothelial mechano-transduction, amplifying low WSS-driven inflammatory signaling.[19] These interactions suggest that systemic metabolic states act as amplifiers of hemodynamic risk, particularly in early stages where PBV-corrected WSS detects subclinical endothelial thickening (Fig. 7). While our study focused on hyperlipidemia-driven viscosity shifts, future work integrating genetic data (e.g., APOE or LDLR polymorphisms) and metabolic biomarkers (e.g., HbA1c and CRP) could refine personalized WSS thresholds for atherosclerosis risk prediction. Such a multifactorial approach may bridge biomechanical and systemic biological factors of vascular pathology.

I. Limitations

While the robustness of PBV method is demonstrated in animal models and phantoms, its direct applicability to human studies requires addressing several key challenges. First, human carotid arteries exhibit greater anatomical complexity compared to rodents and rabbits, including higher curvature variability, frequent branching patterns, and pre-existing atherosclerotic lesions in at-risk populations. The current requirement for straight vessel segments (curvature $<4.6°$) limits analysis in human subjects with tortuous or stenotic arteries. Integrating machine learning, such as physics-informed neural networks, is one potential direction to solve this problem. Second, atherosclerosis risk of human is influenced by broader physiological variability (e.g., anatomical complexity on carotid bifurcations, hematocrit fluctuations, and comorbidities like hypertension), genetic/metabolic factors (e.g., polymorphisms of eNOS or diabetes), and lifestyle factors (e.g., diet and exercise), which may amplify interindividual differences in viscosity–WSS coupling. Integrating multi-omics approaches with advanced hemodynamic modeling holds promise for elucidating these complex interactions, which will be our subsequent work. Third, clinical MRI protocols face challenges such as the excessively long scan time, motion artifacts from patient movement, and low spatial resolution compared to preclinical systems. Accordingly, *in vivo* velocity analysis accuracy can be affected but may be improved with 4D flow acceleration imaging methods.

V. CONCLUSION

The selection of empirical and personalized viscosity has notable impacts on the outcomes of WSS calculations during hemodynamic analysis. In the present study, the proposed methodology enables the *in vivo* measurement of blood flow stress–strain relationships and incorporates individualized blood pressure data from subjects to derive personalized non-Newtonian blood viscosity, which further improves the accuracy in WSS estimated for rats and large animal model and human-artery-like phantoms.

The TAWSS values adjusted with PBV exhibit higher sensitivity compared to hemodynamic analyses that relied solely on empirical viscosity parameters. This finding suggests that variations in blood viscosity, particularly those induced by hyperlipidemia, may play a significant role in the initiation and progression of AS. Consequently, the *in vivo* MRI measurement of blood viscosity reported in the present study may open a new avenue for developing potential preventive and therapeutic strategies fight against AS. Our findings may contribute to a better understanding of the role of blood viscosity during AS development and provide a tool for personalized assessment and early risk stratification in AS patients.

The MATLAB codes for the personalized blood viscosity estimation are available upon request.

SUPPLEMENTARY MATERIAL

See the supplementary material provides detailed protocols for viscosity measurement of the glycerol solution in the phantom experiment, and additional supporting figures not included in the main text.

ACKNOWLEDGMENTS

This work was supported by the National Key Research and Development Program of China (2018YFA0704000), the National Natural Science Foundation of China (U21A20392, 82127802, and 21921004, 22404064), the Hubei Provincial Natural Science Foundation of China (Grant No. 2023BCB092), CAS Youth Interdisciplinary Team (JCTD-2022-13). X. Zhou acknowledges the support from the Tencent Foundation through the XPLORER PRIZE, and S. Chen acknowledges the support from the Young Top-notch Talent Cultivation Program of Hubei Province.

AUTHOR DECLARATIONS

Conflict of Interest

The authors have no conflicts to disclose.

Ethics Approval

Approval of rats ethical and experimental procedures and protocols was granted by the Committee on Animal Research and Ethics of Innovation Academy for Precision Measurement Science and Technology, Chinese Academy of Sciences under Approval No. APM23036A, and approval of rabbits ethical and experimental procedures and protocols was granted by the Experimental Animal Management and Use Committee of the Hubei Provincial Center for Disease Control and Prevention under Approval No. APZX202340206.

Author Contributions

Haiwei Shan: Conceptualization (equal); Data curation (equal); Formal analysis (equal); Investigation (equal); Methodology (equal); Software (equal); Validation (equal); Visualization (equal); Writing – original draft (equal). **Shizhen Chen:** Conceptualization (equal); Data curation (equal); Formal analysis (equal); Supervision (equal); Funding acquisition (equal); Methodology (equal); Project administration (equal); Resources (equal); Writing – review & editing (equal). **Xiaodong Zhang:** Formal analysis (equal); Supervision (equal); Visualization (equal); Writing – original draft (equal). **Haidong Li:** Resources (equal); Software (equal); Writing – review & editing (equal). **Lei Shi:** Resources (equal); Validation (equal); Writing – review & editing (equal). **Xin Zhou:** Data curation (equal); Supervision (equal); Funding acquisition (equal); Project administration (equal); Writing – review & editing (equal).

DATA AVAILABILITY

The data that support the findings of this study are available from the corresponding author upon reasonable request.

REFERENCES

[1]A. J. Lusis, "Atherosclerosis," Nature **407**, 233 (2000).
[2]J. L. M. Björkegren and A. J. Lusis, "Atherosclerosis: Recent developments," Cell **185**, 1630–1645 (2022).
[3]H. Samady, D. S. Molony, A. U. Coskun, A. S. Varshney, B. De Bruyne, and P. H. Stone, "Risk stratification of coronary plaques using physiologic characteristics by CCTA: Focus on shear stress," J. Cardiovasc. Comput. Tomogr. **14**, 386 (2020).
[4]E. M. J. Hartman, G. De Nisco, A. M. Kok, M. Tomaniak, F. M. A. Nous, S.-A. Korteland, F. J. H. Gijsen, W. K. den Dekker, R. Diletti, N. M. D. A. van Mieghem, J. M. Wilschut, F. Zijlstra, A. F. W. van der Steen, R. P. J. Budde, J. Daemen, and J. J. Wentzel, "Wall shear stress-related plaque growth of lipid-rich plaques in human coronary arteries: An near-infrared spectroscopy and optical coherence tomography study," Cardiovasc. Res. **119**, 1021 (2023).
[5]E. M. J. Hartman, G. De Nisco, F. J. H. Gijsen, S.-A. Korteland, A. F. W. van der Steen, J. Daemen, and J. J. Wentzel, "The definition of low wall shear stress and its effect on plaque progression estimation in human coronary arteries," Sci. Rep. **11**, 22086 (2021).
[6]V. Mazzi, G. De Nisco, A. Hoogendoorn, K. Calò, C. Chiastra, D. Gallo, D. A. Steinman, J. J. Wentzel, and U. Morbiducci, "Early atherosclerotic changes in coronary arteries are associated with endothelium shear stress contraction/expansion variability," Ann. Biomed. Eng. **49**, 2606 (2021).
[7]E. Roux, P. Bougaran, P. Dufourcq, and T. Couffinhal, "Fluid shear stress sensing by the endothelial layer," Front. Physiol. **11**, 861 (2020).
[8]S. Rashad, X. Han, K. Saqr, S. Tupin, M. Ohta, K. Niizuma, and T. Tominaga, "Epigenetic response of endothelial cells to different wall shear stress magnitudes: A report of new mechano-miRNAs," J. Cell. Physiol. **235**, 7827–7839 (2020).
[9]A. Woodfin, M. B. Voisin, and S. Nourshargh, "PECAM-1: A multi-functional molecule in inflammation and vascular biology," Arterioscler., Thromb., Vasc. Biol. **27**(12), 2514–2523 (2007).
[10]A. Lai, Y. Zhou, P. Thurgood, C. Chheang, N. C. Sekar, N. Nguyen, K. Peter, K. Khoshmanesh, and S. Baratchi, "Endothelial response to the combined biomechanics of vessel stiffness and shear stress is regulated via Piezo1," ACS Appl. Mater. Interfaces **15**(51), 59103–59116 (2023).
[11]H. H. Carter, C. L. Atkinson, I. H. A. Heinonen, A. Haynes, E. Robey, K. J. Smith, P. N. Ainslie, R. L. Hoiland, and D. J. Green, "Evidence for shear stress–mediated dilation of the internal carotid artery in humans," Hypertension **68**(5), 1217–1224 (2016).
[12]A. Poduri, A. H. Chang, B. Raftrey, S. Rhee, M. Van, and K. Red-Horse, "Endothelial cells respond to the direction of mechanical stimuli through SMAD signaling to regulate coronary artery size," Development **144**, 3241–3252 (2017).
[13]A. Tziotziou, E. Hartman, S. A. Korteland, A. van der Lugt, A. F. W. van der Steen, J. Daemen, D. Bos, J. Wentzel, and A. C. Akyildiz, "Mechanical wall stress and wall shear stress are associated with atherosclerosis development in non-calcified coronary segments," Atherosclerosis **387**, 117387 (2023).
[14]J. Zhou, Y. Li, and S. Chien, "Shear stress-initiated signaling and its regulation of endothelial function," Arterioscler., Thromb., Vasc. Biol. **34**, 2191–2198 (2014).
[15]Y. Zhu, T. Wang, Y. Yang *et al.*, "Low shear stress exacerbates atherosclerosis by inducing the generation of neutrophil extracellular traps *via* Piezo1-mediated mechanosensation," Atherosclerosis **391**, 117473 (2024).
[16]Y. Chen, J. Liu, M. Li, Y. Yu, Z. Yan, W. Shiu, B. Wu, Z. Cheng, Y. Meng, Y. Liu, W. Yuan, Z. Zhang, and W. Xu, "Non-invasive assessment of intracranial wall shear stress using high-resolution magnetic resonance imaging in combination with computational fluid dynamics technique," Fundam. Res. **2**(2), 329–334 (2022).
[17]R. E. Sayed, C. C. Park, Z. Shah, F. B. Nahab, D. C. Haussen, J. W. Allen, and J. N. Oshinski, "Assessment of complex flow patterns in patients with carotid webs, patients with carotid atherosclerosis, and healthy subjects using 4D flow MRI," J. Magn. Reson. Imaging **59**(6), 2001–2010 (2024).
[18]P. Fillingham, N. Belur, R. Sweem, M. C. Barbour, L. M. M. Marsh, A. Aliseda, and M. R. Levitt, "Standardized viscosity as a source of error in computational fluid dynamic simulations of cerebral aneurysms," Med. Phys. **51**(2), 1499 (2024).
[19]M. F. McCarty, J. H. O' Keefe, and J. J. DiNicolantonio, "Pentoxifylline for vascular health: A brief review of the literature," Open Heart **3**, e000365 (2016).
[20]J. Malik, L. Novakova, A. Valerianova, E. Chytilova, V. Lejsek, K. Buryskova Salajova, L. Lambert, T. Grus, M. Porizka, and P. Michalek, "Wall shear stress alteration: A local risk factor of atherosclerosis," Curr. Atheroscler. Rep. **24**(3), 143–151 (2022).
[21]E. Ferdian, D. J. Dubowitz, C. A. Mauger, A. Wang, and A. A. Young, "WSSNet: Aortic wall shear stress estimation using deep learning on 4D flow MRI," Front. Cardiovasc. Med. **8**, 769927 (2022).
[22]W. Chen, M. Xia, W. Zhu, Z. Xu, B. Cai, and H. Shen, "A bio-fabricated tesla valves and ultrasound waves-powered blood plasma viscometer," Front. Bioeng. Biotechnol. **12**, 1394373 (2024).
[23]H. Yi, Z. F. Yang, M. Johnson, L. Bramlage, and B. Ludwig, "Hemodynamic characteristics in a cerebral aneurysm model using non-Newtonian blood analogues," Phys. Fluids **34**, 103101 (2022).
[24]F. D. Auria, L. Centurione, M. A. Centurione, A. Angelini, and R. D. Pietro, "Tumor Necrosis Factor Related Apoptosis Inducing Ligand (Trail) in endothelial response to biomechanical and biochemical stresses in arteries," J. Cell. Biochem. **116**, 2427–2434 (2015).
[25]V. Thondapu, C. V. Bourantas, N. Foin, I. Jang, P. W. Serruys, and P. Barlis, "Biomechanical stress in coronary atherosclerosis: Emerging insights from computational modelling," Eur. Heart J. **38**, 81–92 (2017).
[26]E. M. Cherry and J. K. Eaton, "Shear thinning effects on blood flow in straight and curved tubes," Phys. Fluids **25**, 073104 (2013).

[27]M. Khalifé, A. Decoene, F. Caetano, L. de Rochefort, E. Durand, and D. Rodríguez, "Estimating absolute aortic pressure using MRI and a one-dimensional model," J. Biomech. **47**(13), 3390–3399 (2014).
[28]J. B. Mendieta, D. Fontanarosa, J. Q. Wang, P. K. Paritala, T. McGahan, T. Lloyd, and Z. Y. Li, "The importance of blood rheology in patient-specific computational fluid dynamics simulation of stenotic carotid arteries," Biomech. Model. Mechanobiol. **19**, 1477–1490 (2020).
[29]K. M. Saqr, O. Mansour, S. Tupin, T. Hassan, and M. Ohta, "Evidence for non-Newtonian behavior of intracranial blood flow from Doppler ultrasonography measurements," Med. Biol. Eng. Comput. **57**, 1029–1036 (2019).
[30]N. A. Hem, J. Phie, L. Chilton, and R. Kinobe, "A volume-pressure tail cuff method for hemodynamic parameters: Comparison of restraint and light isoflurane anesthesia in normotensive male Lewis rats," J. Pharmacol. Toxicol. Methods **100**, 106601 (2019).
[31]H. Shan, L. Shi, S. Liu, Y. Yuan, H. Li, S. Chen, and X. Zhou, "A local-saturation-and-delay MRI method for evaluation of red blood cells aggregation *in vivo* for tumor-bearing or drug-used rats," Front. Bioeng. Biotechnol. **11**, 1111840 (2023).
[32]J. F. Jiang and C. M. Strother, "Interactive decomposition and mapping of saccular cerebral aneurysms using harmonic functions: its first application with 'patient-specific' computational fluid dynamics (CFD) simulations," IEEE Trans. Med. Imaging **32**(2), 153–164 (2013).
[33]S. Kotian, N. Methekar, and S. Nikam, "A computational study of the influence of wavy arteries and veins on hemodynamic characteristics in an unsteady state," Phys. Fluids **36**(10), 101912 (2024).
[34]U. M. Sonmez, Y. Cheng, S. C. Watkins, B. L. Roman, and L. A. Davidson, "Endothelial cell polarization and orientation to flow in a novel microfluidic multimodal shear stress generator," Lab Chip **20**(23), 4373–4390 (2020).
[35]Y. Yang, P. Fathi, G. Holland, D. Pan, N. S. Wang, and M. B. Esch, "Pumpless microfluidic devices for generating healthy and diseased endothelia," Lab Chip **19**(19), 3212–3219 (2019).
[36]Y. Sheng, G. Meng, M. Zhang, X. Chen, X. Chai, H. Yu, L. Han, Q. Wang, Y. Wang, and M. Jiang, "Dan-shen Yin promotes bile acid metabolism and excretion to prevent atherosclerosis via activating FXR/BSEP signaling pathway," J. Ethnopharmacol. **330**, 118209 (2024).
[37]X. Nie, R. Laforest, A. Elvington, G. J. Randolph, J. Zheng, T. Voller, D. R. Abendschein, S. E. Lapi, and P. K. Woodard, "PET/MRI of hypoxic atherosclerosis using ^{64}Cu-ATSM in a rabbit model," J. Nucl. Med. **57**(12), 2006–2011 (2016).
[38]A. L. DiCarlo, D. W. Holdsworth, and T. L. Poepping, "Study of the effect of stenosis severity and non-Newtonian viscosity on multidirectional wall shear stress and flow disturbances in the carotid artery using particle image velocimetry," Med. Eng. Phys. **65**, 8–23 (2019).
[39]T. W. Secomb, "Blood flow in the microcirculation," Annu. Rev. Fluid Mech. **49**, 443–461 (2017).
[40]A. R. Pries, D. Neuhaus, and P. Gaehtgens, "Blood viscosity in tube flow: Dependence on diameter and hematocrit," Am. J. Physiol. **263**, H1770–1778 (1992).
[41]S. A. Wajihah and D. S. Sankar, "A review on non-Newtonian fluid models for multi-layered blood rheology in constricted arteries," Arch. Appl. Mech. **93**(5), 1771–1796 (2023).
[42]E. Alay, M. Skotak, S. Chandrasekeran, J. Ziner, and N. Chandra, "Variations in constitutive properties of the fluid elicit divergent vibrational and pressure response under shock wave loading," J. Biomech. Eng. **143**(1), 011003 (2021).
[43]B. Tanczos, V. Somogyi, M. Bombicz, B. Juhasz, N. Nemeth, and A. Deak, "Changes of hematological and hemorheological parameters in rabbits with hypercholesterolemia," Metabolites **11**, 249 (2021).
[44]B. D. Allen, P. J. Aouad, N. S. Burris, A. A. Rahsepar, K. B. Jarvis, C. J. Francois, A. J. Barker, S. C. Malaisrie, J. C. Carr, J. D. Collins, and M. Markl, "Detection and hemodynamic evaluation of flap fenestrations in type B aortic dissection with 4D flow MRI: Comparison with conventional MRI and CTA angiography," Radiology **1**, e180009 (2019).
[45]H. Kamada, M. Nakamura, H. Ota, S. Higuchi, and K. Takase, "Blood flow analysis with computational fluid dynamics and 4D-flow MRI for vascular diseases," J. Cardiol. **80**, 386–396 (2022).
[46]L. J. Leslie, L. J. Marshall, A. Devitt, A. Hilton, and G. D. Tansley, "Cell exclusion in Couette flow: Evaluation through flow visualization and mechanical forces," Artif. Organs. **37**(3), 267–275 (2013).
[47]R. F. Kelly and H. M. Snow, "Characteristics of the response of the iliac artery to wall shear stress in the anaesthetized pig," J. Physiol. **582**, 731–743 (2007).
[48]J. M. Szafron, E. E. Heng, J. Boyd, J. D. Humphrey, and A. L. Marsden, "Hemodynamics and wall mechanics of vascular graft failure," Arterioscler., Throm., Vasc. Biol. **44**, 1065–1085 (2024).
[49]A. Riccio, C. M. A. Cefalo, C. Mazzanti, L. Vero, T. V. Fiorentino, M. Massimino, G. Monea, E. Succurro, M. Perticone, A. Sciacqua, F. Andreozzi, and G. Sesti, "Whole blood viscosity is associated with reduced myocardial mechano-energetic efficiency in nondiabetic individuals," Eur. J. Clin. Invest. **54**, e14127 (2024).
[50]E. Gianos, P. B. Duell, P. P. Toth *et al.*, "Lipoprotein apheresis: Utility, outcomes, and implementation in clinical practice: A scientific statement from the American heart association," Arterioscler., Thromb., Vasc. Biol. **44**, e304–e321 (2024).
[51]S. Lu and S. Zhang, "Atherosclerosis research: The impact of physiological parameters on vascular wall stress," SN Appl. Sci. **1**, 692 (2019).
[52]R. T. Fernández, C. Tristão-Pereira, J. C. Silla-Castro *et al.*, "Apolipoprotein E–ε2 and resistance to atherosclerosis in midlife: The PESA observational study," Circ. Res. **134**, 411–424 (2024).
[53]R. S. Rosenson, M. L. Lee, and Q. Chen, "Association of total VLDL particle concentrations with elevated blood viscosity in patients with type 2 diabetes," Diabetes Res. Clin. Pract. **183**, 109180 (2022).
[54]C. Strecker, A. J. Krafft, L. Kaufhold *et al.*, "Carotid geometry and wall shear stress independently predict increased wall thickness—A longitudinal 3D MRI study in high-risk patients," Front. Cardiovasc. Med. **8**, 723860 (2021).
[55]A. Briole, T. Podgorski, and B. Abou, "Molecular rotors as intracellular probes of red blood cell stiffness," Soft Matter **17**, 4525–4537 (2021).
[56]E. Nader, C. Nougier, C. Boisson *et al.*, "Increased blood viscosity and red blood cell aggregation in patients with COVID-19," Am. J. Hematol. **97**, 283–292 (2022).
[57]J. Fan and T. Watanabe, "Atherosclerosis: Known and unknown," Pathol. Int. **72**, 151–160 (2022).
[58]X. Zhang, S. Leng, X. Liu, X. Hu, Y. Liu, X. Li, Q. Feng, W. Guo, N. Li, Z. Sheng, S. Wang, and J. Peng, "Ion channel Piezo1 activation aggravates the endothelial dysfunction under a high glucose environment," Cardiovasc. Diabetol. **23**, 150 (2024).
[59]N. D. Thien, N. Hai-Dam, D. T. Anh, and D. Baecker, "Piezo1 and its inhibitors: Overview and perspectives," Eur. J. Med. Chem. **273**, 116502 (2024).
[60]T. Konsola, G. Siasos, A. S. Antonopoulos *et al.*, "The impact of T786C and G894T polymorphisms of eNOS on vascular endothelial growth factor serum levels in type 2 diabetes patients," Int. J. Cardiol. **222**, 155–156 (2016).